SCIENTIFIC REP🔴RTS

Lithium intercalation mechanism into FeF$_3$·0.5H$_2$O as a highly stable composite cathode material

Ghulam Ali[1], Ji–Hoon Lee[1], Wonyoung Chang[1], Byung-Won Cho[1], Hun-Gi Jung[1], Kyung-Wan Nam[2] & Kyung Yoon Chung[1]

The growing demand for lithium-ion batteries (LIBs) requires investigation of high-performance electrode materials with the advantages of being environmentally friendly and cost-effective. In this study, a nanocomposite of open-pyrochlore-structured FeF$_3$·0.5H$_2$O and reduced graphene oxide (RGO) is synthesized for use as a high-performance cathode in LIBs, where RGO provides high electrical conductivity to the composite material. The morphology of the composite shows that FeF$_3$·0.5H$_2$O spheres are embedded into RGO layers and high-resolution TEM image shows that those spheres are composed of primary nanoparticles with a size of ~5 nm. The cycling performance indicates that the composite electrode delivers an initial high discharge capacity of 223 mAh g^{-1} at 0.05 C, a rate capability up to a high C-rate of 10 C (47 mAh g^{-1}) and stable cycle performance at 0.05 C (145 mAh g^{-1} after 100 cycles) and 0.2 C (93 mAh g^{-1} after 100 cycles) while maintaining high electrochemical reversibility. Furthermore, the responsible electrochemical reaction is investigated using *in-situ* XRD and synchrotron-based X-ray absorption spectroscopy (XAS), and the XRD results show that FeF$_3$·0.5H$_2$O transitions to an amorphous-like phase through a lithiation process. However, a reversible oxidation change of Fe^{3+} ↔ Fe^{2+} is identified by the XAS results.

Widespread energy consumption and environmental concerns over fossil fuels require advances in electrochemical energy storage systems ranging from portable to large-scale applications[1–3]. In this regard, the development of high-performance electrode materials for lithium-ion batteries (LIBs) is needed to meet the rapidly increasing demand for energy storage devices. There are plenty of anode materials which show promising electrochemical performance in LIBs such as carbonaceous materials, de/alloying based materials, metal oxides, metal oxyfluorides, etc.[4,5]. Unfortunately, the commercially available LIBs for portable devices have adopted cobalt-based cathode materials, which have the drawback of high fabrication costs, especially for large-scale applications[6]. Therefore, the main interest in the development of LIBs is to identify electrode materials that are cost-effective while maintaining the energy and power densities of the batteries. Metal fluorides are promising cathode materials due to their high theoretical capacities based on the multiple electron redox reaction and higher working potential than sulfides, nitrides and oxides[7,8]. Due to the abundance and low cost of iron, FeF$_3$ is the most suitable candidate among the various types of metal fluorides. FeF$_3$ exhibits high capacity (237 mAh g^{-1} for one-electron transfer and 712 mAh g^{-1} for three-electron transfer) and high working potential (>3.0 V for the Fe^{2+}/Fe^{3+} redox reaction)[9,10]. Moreover, FeF$_3$ is a better choice for Li-polymer batteries where Li metal is used as the anode[11]. Despite the high capacity and working potential, FeF$_3$ is intrinsically an insulator due to the high iconic character of the metal-halogen bonds, and the poor kinetics limit its capacity[7]. High electrochemical activity can be achieved by reducing the particle size to the nanometer scale and by providing electronic conductive networks[11,12]. The combination of these approaches shortens the ion transport distance into the electrode and enhances the electrochemical performance of the FeF$_3$ cathode[12–14]. As a conductive network, graphene possesses several advantages over other carbonaceous materials, such as high electric conductivity, large surface area (2630 m^2 g^{-1}), high thermal stability, and superior mechanical flexibility[15–18].

The crystal structure is an important factor in the electrochemical performance of the electrode material for battery applications. FeF$_3$, with or without hydrate contents, is found with several crystal structures, including

[1]Center for Energy Convergence Research, Korea Institute of Science and Technology, Hwarang–ro 14–gil 5, Seongbuk–gu, Seoul 02792, Republic of Korea. [2]Department of Energy and Materials Engineering, Dongguk University, Seoul 04620, Republic of Korea. Correspondence and requests for materials should be addressed to K.-W.N. (email: knam@donggok.edu) or K.Y.C. (email: kychung@kist.re.kr)
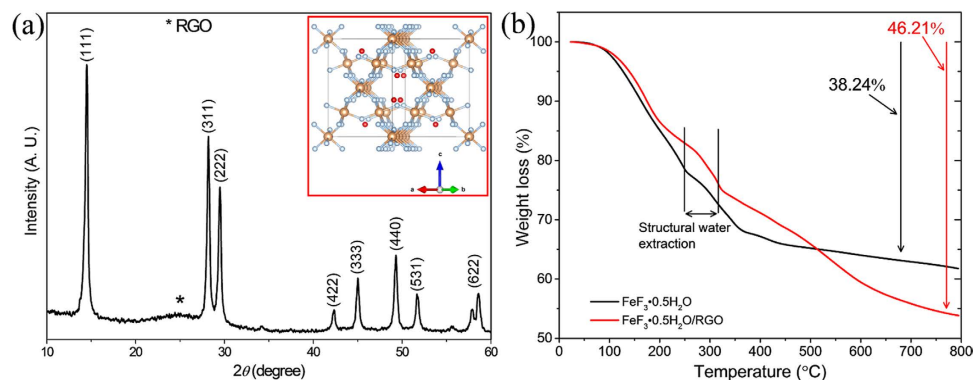
Figure 1. Structural characterization of FeF$_3$·0.5H$_2$O/RGO composite. (**a**) XRD pattern of the FeF$_3$·0.5H$_2$O/RGO composite (the asterisk (*) denotes the RGO peak). The inset shows the crystal structure of pyrochlore FeF$_3$·0.5H$_2$O, where Fe atoms are shown in gray, F atoms in blue and H$_2$O molecules in red, located in a zigzag position in structure. (**b**) Thermogravimetric analysis data of the bare FeF$_3$·0.5H$_2$O and RGO composite.

cubic pyrochlore with the Fd3m space group[19], tetragonal with the P4/n space group[20], orthorhombic ReO$_3$-type with the Cmcm space group[21], and rhombohedral-type with the R-3c space group[22], hexagonal tungsten bronze-type with the Cmcm space group[22]. Cubic pyrochlore FeF$_3$ has the advantage of the largest unit cell volume of 1100.7 Å^3 with large open tunnels[22]. Therefore, this FeF$_3$ pyrochlore provides a high rate of alkali ion insertion/extraction. In addition, hydrated forms of iron fluorides (FeF$_3$·xH$_2$O) have recently been introduced with structural and morphological advantages[23–25]. FeF$_3$·0.5H$_2$O has an open pyrochlore structure (*Fd-3m* space group) and a large unit cell volume (1127 Å^3), which are beneficial for the facile intercalation of alkali ions[26–28]. The pyrochlore-type FeF$_3$·0.5H$_2$O composite with single-walled nanotubes (SWNTs) has shown a stable capacity of 135 mAh g^{-1} in LIBs[27]. Reduced graphene oxide (RGO) has been used to increase the electrical conductivity of cathode materials that suffer from poor conductivities and to ensure a uniform distribution of particles on the surface and between the layers of graphene[29–31]. Furthermore, the high thermal stability of RGO helps the composites to withstand high current loads, where heat generation in the cells is significant[32].

The aim of this study is to synthesize an RGO and FeF$_3$·0.5H$_2$O composite with the advantage of the particle size reduced to a few nanometers. The composite electrode is used as a cathode in LIBs, where its cycle and rate capability are measured under different current densities. Furthermore, the electrochemical reaction mechanism of Li$^+$ insertion/extraction into FeF$_3$·0.5H$_2$O is investigated by *in-situ* x-ray diffraction (XRD) and x-ray absorption spectroscopy (XAS), which provide useful information about the structural changes.

Results

Figure 1 shows the XRD pattern of the synthesized FeF$_3$·0.5H$_2$O/RGO composite. The peaks match those of pyrochlore (*Fd-3m* space group) FeF$_3$·0.5H$_2$O, and the details of its crystal structure (as shown in the inset of Fig. 1) are reported elsewhere[26]. The lattice parameter and volume of the cubic FeF$_3$·0.5H$_2$O are a = 10.405 Å and V = 1126 Å^3, respectively. FeF$_3$·0.5H$_2$O exhibiting the open-framework structure with a large unit cell facilitates cation insertion through the 3D interconnected channels. An RGO peak can also be observed in the XRD pattern with a lower intensity (marked with asterisk (*) symbol), indicating an amorphous-like structure, and it was confirmed that the amount of RGO was ~11 wt% based on the C/S analysis. Thermogravimetric analysis (TGA) was conducted in order to observe the extraction of crystal structure water contents and to determine the amount of RGO in the composite. Figure 1b shows the TGA data of bare and composite FeF$_3$·0.5H$_2$O powders. Both the bare FeF$_3$·0.5H$_2$O and RGO composite materials show that the extraction of structural water occur in the temperature range of 248–315 °C which is comparable to literature[26]. A total weight loss of 38.14% was recorded in case of bare FeF$_3$·0.5H$_2$O at a temperature of 800 °C while it was recorded 46.21% for FeF$_3$·0.5H$_2$O/RGO composite. The composite material shows ~8% more weight loss compare to bare at a temperature of 800 °C which indicates the presence of carbon contents. However, this value of 8 wt.% is lower compare to the value determined by C/S analysis (11 wt.%). This is due to the fact that the bare material also contains carbon contents from the residue of ionic liquid as reported earlier[26].

Figure 2a shows the morphology of FeF$_3$·0.5H$_2$O particles dispersed in the RGO layers, and the average size of the particles is less than 100 nm. The FeF$_3$·0.5H$_2$O particles are strongly bound to RGO. In the composite, RGO has a versatile role: RGO facilitates the electronic conduction of the composite, and its multilayer character lowers the particle-particle interface resistance because the particles are well-scattered. The uniform distribution of FeF$_3$·0.5H$_2$O particles, enabled by the introduction of RGO layers, is expected to increase the rate capability and energy storage capacity of the active material because it can provide more active sites to interact with the electrolyte. TEM imaging of the composite indicates that FeF$_3$·0.5H$_2$O particles are grown between the RGO layers, as shown in Fig. 2b. The high-magnification TEM image shows that each single particle comprises multiple nanoparticles with a size of ~5 nm, as marked by the arrows in Fig. 2c. The nanosized particles decrease the diffusion length of the cation during insertion/extraction into the structure.

The reaction mechanism of the composite cathode was evaluated by cyclic voltammetry (CV), and the measurements were performed at a scan rate of 0.2 mV s^{-1} over a voltage range of 1.7–4.5 V. Figure 3a shows the CV of the composite electrode and one pair of peaks corresponding to the reduction (Li insertion) and oxidation
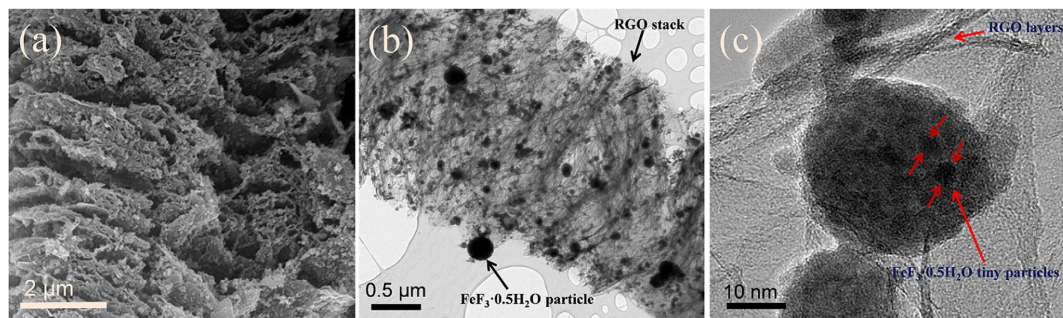
Figure 2. Morphological and microstructural characterizations. (**a**) SEM image of the composite. TEM images (**b**) at low and (**c**) high magnification. The red-colored arrows indicate the size of the $FeF_3 \cdot 0.5H_2O$ nanoparticles.

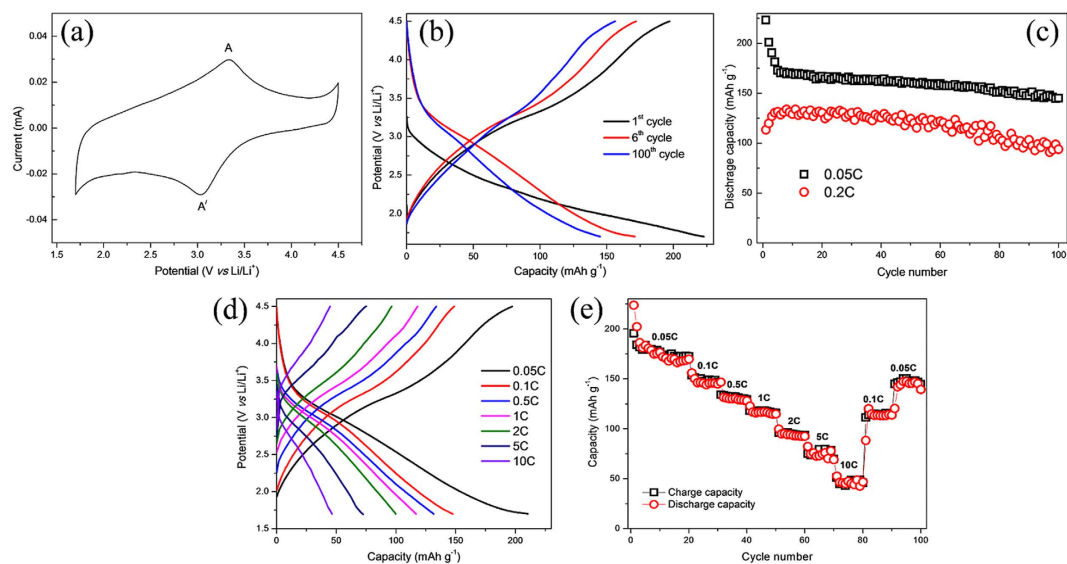**Figure 3. Electrochemical performance of the $FeF_3 \cdot 0.5H_2O$/RGO composite cathode.** (**a**) Cyclic voltammograms of the $FeF_3 \cdot 0.5H_2O$/RGO composite at a scan rate of 0.2 mV s^{-1}. (**b**) Potential profiles of the composite at a rate of 0.05 C for the 1st, 6th and 100th cycle. (**c**) Discharge capacity as a function of cycle number at a C-rate of 0.05 and 2 C. (**d**) Potential profiles at current rates of 0.05, 0.1, 0.5, 1, 2, 5, and 10 C. (**e**) Specific capacity versus cycle number at current rates of 0.05, 0.1, 0.5, 1, 2, 5, and 10 C.

(Li extraction) peaks located at 3.03 V and 3.33 V, respectively. We believe that these value can be correlated to the average working potential during discharging and charging, respectively. The redox peak (A/A′) reveals the reversible reduction-oxidation of Fe (Fe^{3+}/Fe^{2+}) during cycling.

Figure 3b shows the galvanostatic charge/discharge profile of the composite cathode in a voltage range of 1.7–4.5 V. The first discharge curve exhibits a large capacity of 223 mAh g^{-1} at a rate of 0.05 C (1C = 220 mAh g^{-1}) with a sloping potential profile. This capacity is larger than the theoretical capacity of $FeF_3 \cdot 0.5H_2O$ (220 mAh g^{-1} with one lithium insertion), presumably because of the side reactions on the surface of electrode where redox reaction or ion adsorption occurs at functional groups on the surface of ionic-liquid treated RGO[33]. The potential profile of the composite material stabilizes after a few cycles and delivers a discharge capacity of 171 mAh g^{-1} at the 6th cycle, with a plateau at ~2.9 V. The obtained capacity of our cathode is superior to the literature values of ~110 mAh g^{-1} and 135 mAh g^{-1} [14,27]. This stabilized value of reversible capacity (171 mAh g^{-1}) corresponds to 78% of the theoretical capacity which is calculated on the basis of the active electrode material. We speculate that the electrode material cannot achieve full theoretical capacity presumably due to the presence of water molecules in the structure. The cycle performance of the material is expected to be stable as the electrode material contains water molecules which steadily forms LiOH on the surface to stabilize the reversible de/lithiation process. The cycling stability of the composite at current densities of 0.05 C and 2 C is shown in Fig. 3c. At 0.05 C, the discharge capacity is stabilized after the 5th cycle, and the composite exhibits stable capacities from the 6th cycle. After 100 cycles, the electrode still delivers a high discharge capacity of 145 mAh g^{-1}, which corresponds to a capacity retention of 85% of the stable capacity (171 mAh g^{-1}). For a cell cycled at 0.2 C, a relatively lower initial capacity of 113 mAhg^{-1} is observed. However, the delivered capacity gradually increased within the early stage of cycling and the capacity reached 129 mAh g^{-1} at the 4th cycle. The increase of capacity in the initial cycles is attributed to
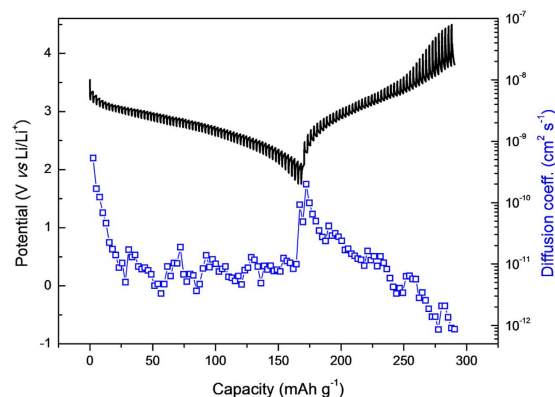
Figure 4. Diffusion coefficient measurement. GITT curve of the $FeF_3 \cdot 0.5H_2O$/RGO composite along with the Li^+ diffusion coefficient as a function of capacity.

the gradual activation of the material under the high current rate of 0.2 C. The electrode delivers a capacity of 94 mAh g^{-1} after 100 cycles, corresponding to a capacity retention of 72%.

To investigate the power performance of the composite cathodes, the charge/discharge profile as the C-rate changes from 0.05 C to 10 C is shown Fig. 3d. The composite cathode material delivered average discharge capacities of 178, 147, 132, 117, 94, 75 and 47 mAh g^{-1} at current rates of 0.05, 0.1, 0.5, 1, 2, 5 and 10 C, respectively. To the best of our knowledge, this is the first report of high rate performance for a pyrochlore $FeF_3 \cdot 0.5H_2O$ cathode. The active material loading and electrode thickness are important factors for electrochemical measurements and high thickness could seriously limits the Li^+ diffusivity and rate performance[34]. The material showed excellent rate performance at high current rates, and even after deep cycling, the recovered average discharge capacity was 112 and 142 mAh g^{-1} at current rates of 0.1 and 0.05 C, respectively. Overall, the composite electrode shows good electrochemical performance, which is attributed to the nanostructure of the $FeF_3 \cdot 0.5H_2O$ and the facile electrolyte and electron conducting network obtained by the addition of RGO. An RGO-only electrode was assembled to observe its contribution to the capacity, and the electrodes were prepared with the same experimental conditions as for the composite material. The RGO electrode exhibits a stable discharge capacity of 95 mAh g^{-1} at rate of 0.05 C. However, because the composite electrode contains only 11 wt% RGO, it contributes negligible capacity to the composite's performance.

The electrochemical performance of an electrode material depends on the alkali insertion/extraction process and galvanostatic intermittent titration technique (GITT) is considered as the most reliable technique to determine the Li diffusivity[35]. We performed GITT to determine the diffusion coefficient of lithium ions (D_{Li}) through the composite electrode at a current density of 0.1 C within a voltage range of 1.7–4.5 V, as shown in Fig. 4. A current was applied for 10 min per each titration during discharge/charge process, with an open-circuit stand for 60 min to allow the cell potential to reach a new steady-state potential. D_{Li} was calculated by assuming that the lithium diffusion in the electrode obeys Fick's law. The overpotential progressively increased with the discharging depth, and D_{Li} decreased from 5.3×10^{-10} (at the start of the discharge process) to 9.9×10^{-12} (at the end of the discharge process) cm^2 s^{-1}. The graph shows a large overpotential of ~3.5 V, which is the starting point of the plateau during the charge process. The D_{Li} value is 2×10^{-10} cm^2 s^{-1} at the beginning and its decreases to 8.7×10^{-13} cm^2 s^{-1} as the potential increases to 4.5 V. The discrepancy in the D_{Li} values at the beginning and after a complete cycle is related to the structural changes and will be explored in later sections. There is no previous report for D_{Li} in pyrochlore-structured $FeF_3 \cdot 0.5H_2O$; however, these calculated values of D_{Li} are consistent with those of $FeF_3 \cdot 3H_2O$, $FeF_3 \cdot 0.33H_2O$, FeF_3/C and FeF_3/graphene[23,36]. Furthermore, the D_{Li} values of our composite are comparable to that of monoclinic Nb_2O_5 (10^{-13}–10^{-12} cm^2 s^{-1}) but higher than pseudo-hexagonal (10^{-17}–10^{-16} cm^2 s^{-1}) and orthorhombic (10^{-15}–10^{-14} cm^2 s^{-1}) Nb_2O_5 phases[37]. Nano-sized layered anode materials such as $Li(Li_{1/3}Ti_{5/3})O_4$ has shown better lithium kinetics and the D_{Li} was calculated to be in the range of 10^{-11}–10^{-9} cm^2 s^{-1} of the cell running at 0.2 C rate[38]. The higher values of D_{Li} at the beginning of discharge/charge process indicate fast Li^+ extraction/insertion into the nanoparticles; however, the D_{Li} values indicate more sluggish behavior with depth in the discharge/charge process, which presumably corresponds to the structural arrangement.

In-situ X-ray diffraction was conducted to observe the phase changes of the material during the discharge/charge process. A coin cell with a hole in the stainless steel part was used to allow the X-ray to be easily injected into the cathodes, and the cell was discharged/charged at a current density of 0.05 C over a voltage range of 1.7–4.5 V. Figure 5a shows the XRD scans in 2θ ranges of 14.2–15.7° and 27–30.5°, where the major (highest intensity) peaks are located. The corresponding discharge profile is shown in Fig. 5b. As the insertion of Li proceeds, the intensity the diffraction peaks decreases, indicating phase transformation of the material towards a poor crystalline state. No significant shift is observed in the peaks. The poor crystallinity of the material is associated with the nanosized particles and the extraction of the water contents from the structure upon Li^+ insertion. The latter phenomenon was previously observed in the case of sodium insertion into pyrochlore $FeF_3 \cdot 0.5H_2O$[26]. The lack of change in the 2θ values during the discharge process can be explained by assuming that Li^+ insertion and water extraction occur simultaneously. The charge process also shows depressed diffraction peaks, and after complete charging and the 2nd discharge process, the peaks are not recovered to the initial state. The irreversibility
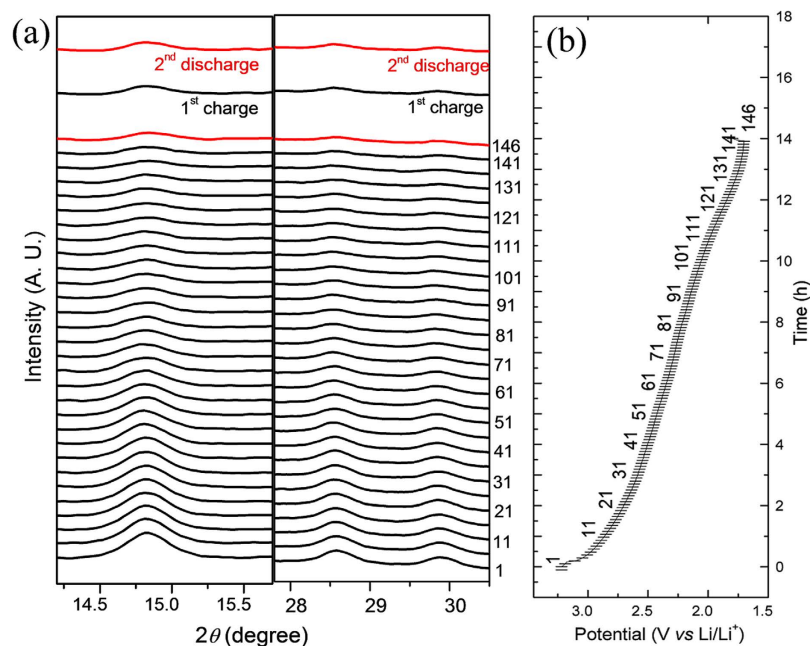
Figure 5. Structural investigation during lithium insertion process using *in-situ* XRD. (**a**) *In-situ* XRD of the composite electrode during the 1st discharge along with the final XRD scans of the 1st charge and 2nd discharge. (**b**) The corresponding curve during the 1st discharge process.

of the diffraction peaks shows that the material is not recovered after reacting with lithium. Amorphization of the material upon Li^+ extraction/insertion is a possible cause of the capacity fade in the initial cycles, and it also causes high polarization, as observed by the GITT analysis.

To identify the changes in electronic structure of the composite electrode during the charging/discharging process, *in-situ* XANES analysis was performed, and the results are depicted in Fig. 6. The cell was discharged/ charged at a rate of 0.1 C in the voltage range of 1.7–4.5 V, and the resulting profile is marked with number where the XANES spectra were measured (Fig. 6a). Figure 6b and c show the Fe K-edge *in-situ* XANES spectra of the composite electrode during the discharge and charge processes, respectively. The XANES spectra of the standard samples for 2+ (FeF_2) and 3+ (FeF_3) were also measured to observe the total valence change of Fe in the composite electrode. The absorption edge of FeF_2 is at 7121.5 eV, and it is at a higher energy for FeF_3 (7127 eV). The 1st XANES spectrum (Fig. 6b) is at slightly lower energy than FeF_3 because of the position of the scan on the charge-discharge curve, as shown in Fig. 6a. The XANES spectra of the composite electrode systematically shift to lower energies as the depth of discharge increases. At the fully discharged state (point 8), the edge energy (inflection point) almost overlaps that of the reference 2+, revealing the average valence state of Fe was reduced from 3+ to 2+. During the following charge process (Fig. 6c), a reversed tendency of the shift in the XANES spectra is observed, which reveals the oxidation of Fe upon the extraction of Li^+. The XANES spectrum of the fully charged electrode (no. 15) is at slightly lower energy compared to FeF_3 (standard), which may be due to intercalation of Li into $FeF_3 \cdot 0.5H_2O$ and changes in the structure, as already evidenced by the GITT and *in-situ* XRD results. Overall, the XANES results show that the capacity contribution in the composite is mainly due to the oxidation/reduction of Fe between 2+ and 3+.

To further investigate the reaction mechanism, Fourier-transformed (FT) k^2-weighted Fe K-edge extended x-ray absorption fine structure (EXAFS) spectra of the selected scans (Fig. 6d) are plotted along with Fe metal foil, and the data are not phase-corrected. The first spectrum (point 1) shows two distinct peaks at approximately 0.152 and 0.311 nm, which correspond to Fe-F and Fe-Fe bonding, respectively. A significant change was observed in the intensity of the peaks during the discharge/charge process. However, no significant peak of Fe metal was observed during cycling, which suggests the reaction did not proceed through a conversion mechanism.

Discussion

The Fe-based, low-cost, earth-abundant, environmentally benign nanocomposite showed high electrochemical performance as a cathode in SIBs, where it exhibits a high discharge capacity of 223 mAh g^{-1} in the initial cycle and 145 mAh g^{-1} at the 100th cycle at a rate of 0.05 C and operates at high rate of 10 C (delivers 47 mAh g^{-1}). The excellent electrochemical performance of the composite is attributed to the (i) the open-framework cubic-pyrochlore-type crystal structure, (ii) the nanostructure of the $FeF_3 \cdot 0.5H_2O$, which offers a short diffusion path for Li^+ and (iii) the incorporation of RGO, which results in high rate capabilities, indicative of the positive synergistic effect on $FeF_3 \cdot 0.5H_2O$ and the RGO composite. Our work shows that the composite material containing RGO and ultra-small nanoparticles with a size of ~5 nm can improve LIB performance. Furthermore, a facile co-precipitation synthesis method at room temperature makes it possible to minimize the processing costs during industrial production. This study employs a variety of methods to observe the structural evolution of the
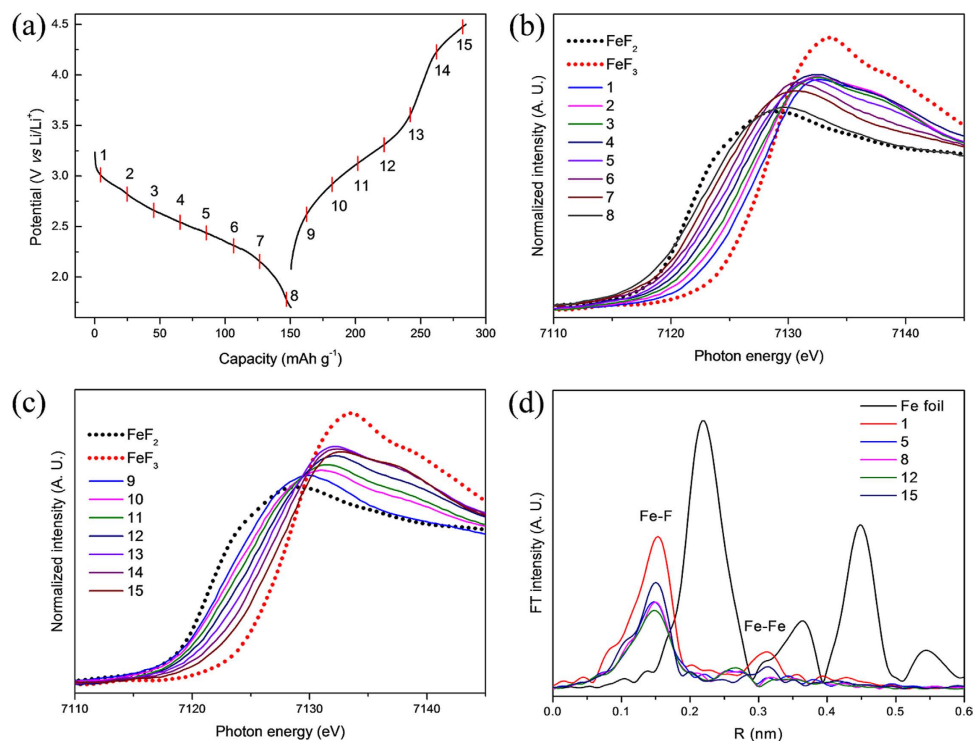
Figure 6. Lithium storage mechanism using *in-situ* XAS. (**a**) Potential process marked with numbers on the profile where the XANES spectra are measured. (**b**) *In-situ* XANES of the composite electrode during the discharge process and (**c**) charge process. (**d**) Selected EXAFS spectra during the discharge/charge process are plotted along with Fe metal foil.

composite material during Li^+ insertion/extraction, including GITT, *in-situ* XRD and XANES. The *in-situ* XRD results reveal that lithium insertion into the composite results in poor crystallinity of the material. The XANES study shows that Fe valence systematically changes from 3+ to 2+ during the discharge process and vice versa.

Methods

$Fe(NO_3)_3 \cdot 9H_2O$ (Aldrich Korea, 99.99%) and ionic liquid 1-butyl-3-methylimidazolium tetrafluoroborate ($BMIMBF_4$) (Aldrich, >98%) were used in the synthesis of $FeF_3 \cdot 0.5H_2O$ along with reduced graphene oxide. The synthesis of $FeF_3 \cdot 0.5H_2O/RGO$ was recently reported[26]. We modified the process by reducing the amount of reduced graphene oxide and decreasing the reaction time to 8 h to obtain the uniform growth of particles with controlled size.

Characterizations. The crystal structure of the composite was characterized with a Rigaku X-ray diffractometer with Cu-Kα radiation. The morphology of the composite was observed by scanning electron microscopy (Fe-SEM, NOVA NanoSEM200, FEI). The microstructure of the composite was observed by transmission electron spectroscopy (TEM, Tecnai G^2 F20 FEI).

Electrochemical tests. The electrodes were prepared by mixing the composite, carbon black and polyvinylidene difluoride (PVdF) at a weight ratio of 7:2:1. The mixture was pasted on aluminum foil, roll-pressed and vacuum-dried at 80 °C overnight. The composite electrodes with a thickness of ~30 μm and an active material weight of ~1.8 mg were used to make coin cells, and 1 M $LiPF_6$ dissolved in ethylene carbonate, diethyl carbonate and dimethyl carbonate at a volume ratio of 1:1:1 was used as the electrolyte. Lithium foil was used as the counter electrode.

In-situ XRD and XANES. A CR 2032 coin cell with 3 mm hole in its solid part was used for the *in-situ* XRD measurements (R–AXIS IV++, Rigaku) at the Korea Institute of Science and Technology (KIST). The cell was galvanostatically cycled at a current density of 0.05 C through a voltage range of 1.7–4.5 V using a Wonatech battery test system (WBCS 3000K8). The data were recorded with Mo–Kα radiation ($\lambda = 0.7107$ Å) and later converted to Cu–Kα radiation ($\lambda = 1.54$ Å).

XANES measurements were performed at the KIST–PAL 1D beamline of the Pohang Light Source (PLS–II), and a Si(111) double crystal monochromator was used for energy selection. The Fe K-edge (7112 eV) spectra were measured in transmission mode, and a pure iron foil was used as reference to calibrate the spectra. A Gamry instrument (Reference 600™) was used for the galvanostatic cycling of the laboratory-designed coin cell, and the cell was cycled at a current density of 0.05 C over a voltage range of 1.7–4.5 V. The XANES data were analyzed using the ATHENA package[39]. It is worthy to mention that both *in-situ* XRD and XANES measurements were taken during 1st galvanostatic dis/charge process.

References

1. Yang, Z. G. *et al.* Electrochemical Energy Storage for Green Grid. *Chem Rev* **111,** 3577–3613 (2011).
2. Muldoon, J., Bucur, C. B. & Gregory, T. Quest for Nonaqueous Multivalent Secondary Batteries: Magnesium and Beyond. *Chem Rev* **114,** 11683–11720 (2014).
3. Muhammad, S. *et al.* Evidence of reversible oxygen participation in anomalously high capacity Li- and Mn-rich cathodes for Li-ion batteries. *Nano Energy* **21,** 172–184 (2016).
4. Reddy, M. V., Subba Rao, G. V. & Chowdari, B. V. R. Metal Oxides and Oxysalts as Anode Materials for Li Ion Batteries. *Chem Rev* **113,** 5364–5457 (2013).
5. Reddy, M. V., Madhavi, S., Subba Rao, G. V. & Chowdari, B. V. R. Metal oxyfluorides TiOF2 and NbO2F as anodes for Li-ion batteries. *J Power Sources* **162,** 1312–1321 (2006).
6. Wu, F. *et al.* Multifunctional AlPO4 Coating for Improving Electrochemical Properties of Low-Cost Li[Li0.2Fe0.1Ni0.15Mn0.55]O2 Cathode Materials for Lithium-Ion Batteries. *Acs Appl Mater Inter* **7,** 3773–3781 (2015).
7. Badway, F., Pereira, N., Cosandey, F. & Amatucci, G. G. Carbon-Metal Fluoride Nanocomposites: Structure and Electrochemistry of FeF3: C. *Journal of The Electrochemical Society* **150,** A1209–A1218 (2003).
8. Arico, A. S., Bruce, P., Scrosati, B., Tarascon, J. M. & Van Schalkwijk, W. Nanostructured materials for advanced energy conversion and storage devices. *Nat Mater* **4,** 366–377 (2005).
9. Conte, D. & Pinna, N. A review on the application of iron(III) fluorides as positive electrodes for secondary cells. *Mater Renew Sustain Energy* **3,** 1–22 (2014).
10. Ma, D. L. *et al.* Three-dimensionally ordered macroporous FeF3 and its *in situ* homogenous polymerization coating for high energy and power density lithium ion batteries. *Energ Environ Sci* **5,** 8538–8542 (2012).
11. Ma, D. L. *et al.* *In situ* generated FeF3 in homogeneous iron matrix toward high-performance cathode material for sodium-ion batteries. *Nano Energy* **10,** 295–304 (2014).
12. Kim, S. W., Seo, D. H., Gwon, H., Kim, J. & Kang, K. Fabrication of FeF3 Nanoflowers on CNT Branches and Their Application to High Power Lithium Rechargeable Batteries. *Adv Mater* **22,** 5260–5264 (2010).
13. Li, T., Li, L., Cao, Y. L., Ai, X. P. & Yang, H. X. Reversible Three-Electron Redox Behaviors of FeF3 Nanocrystals as High-Capacity Cathode-Active Materials for Li-Ion Batteries. *J Phys Chem C* **114,** 3190–3195 (2010).
14. Li, C. L., Mu, X. K., van Aken, P. A. & Maier, J. A High-Capacity Cathode for Lithium Batteries Consisting of Porous Microspheres of Highly Amorphized Iron Fluoride Densified from Its Open Parent Phase. *Adv Energy Mater* **3,** 113–119 (2013).
15. Novoselov, K. S. *et al.* Two-dimensional gas of massless Dirac fermions in graphene. *Nature* **438,** 197–200 (2005).
16. Stoller, M. D., Park, S. J., Zhu, Y. W., An, J. H. & Ruoff, R. S. Graphene-Based Ultracapacitors. *Nano Lett* **8,** 3498–3502 (2008).
17. Balandin, A. A. *et al.* Superior thermal conductivity of single-layer graphene. *Nano Lett* **8,** 902–907 (2008).
18. Fasolino, A., Los, J. H. & Katsnelson, M. I. Intrinsic ripples in graphene. *Nat Mater* **6,** 858–861 (2007).
19. Calage, Y. *et al.* Mössbauer study of the new pyrochlore form of FeF3. *J Solid State Chem* **69,** 197–201 (1987).
20. Burbano, M. *et al.* Anionic Ordering and Thermal Properties of FeF3·3H2O. *Inorg Chem* **54,** 9619–9625 (2015).
21. Leblanc, M., Ferey, G., Chevallier, P., Calage, Y. & De Pape, R. Hexagonal tungsten bronze-type FeIII fluoride: (H2O)0.33·FeF3; crystal structure, magnetic properties, dehydration to a new form of iron trifluoride. *J Solid State Chem* **47,** 53–58 (1983).
22. Louvain, N. *et al.* One-shot versus stepwise gas-solid synthesis of iron trifluoride: investigation of pure molecular F2 fluorination of chloride precursors. *Cryst Eng Comm* **15,** 3664–3671 (2013).
23. Liu, L. *et al.* A comparison among FeF3·3H(2)O, FeF3·0.33H(2)O and FeF3 cathode materials for lithium ion batteries: Structural, electrochemical, and mechanism studies. *J Power Sources* **238,** 501–515 (2013).
24. Li, B. J., Rooney, D. W., Zhang, N. Q. & Sun, K. N. An *In Situ* Ionic-Liquid-Assisted Synthetic Approach to Iron Fluoride/Graphene Hybrid Nanostructures as Superior Cathode Materials for Lithium Ion Batteries. *Acs Appl Mater Inter* **5,** 5057–5063 (2013).
25. Li, C. L., Gu, L., Tong, J. W. & Maier, J. Carbon Nanotube Wiring of Electrodes for High-Rate Lithium Batteries Using an Imidazolium-Based Ionic Liquid Precursor as Dispersant and Binder: A Case Study on Iron Fluoride Nanoparticles. *Acs Nano* **5,** 2930–2938 (2011).
26. Ali, G. *et al.* An open-framework iron fluoride and reduced graphene oxide nanocomposite as a high-capacity cathode material for Na-ion batteries. *Journal of Materials Chemistry A* **3,** 10258–10266 (2015).
27. Li, C. L. *et al.* An FeF3·0.5H(2)O Polytype: A Microporous Framework Compound with Intersecting Tunnels for Li and Na Batteries. *J Am Chem Soc* **135,** 11425–11428 (2013).
28. Ali, G. *et al.* Probing the Sodiation-Desodiation Reactions in Nano-sized Iron Fluoride Cathode. *Electrochim Acta* **191,** 307–316 (2016).
29. Mahadi, N. B. *et al.* Vanadium dioxide – Reduced graphene oxide composite as cathode materials for rechargeable Li and Na batteries. *J Power Sources* **326,** 522–532 (2016).
30. Yang, S. B., Feng, X. L., Ivanovici, S. & Mullen, K. Fabrication of Graphene-Encapsulated Oxide Nanoparticles: Towards High-Performance Anode Materials for Lithium Storage. *Angew Chem Int Edit* **49,** 8408–8411 (2010).
31. Kucinskis, G., Bajars, G. & Kleperis, J. Graphene in lithium ion battery cathode materials: A review. *J Power Sources* **240,** 66–79 (2013).
32. Novoselov, K. S. *et al.* A roadmap for graphene. *Nature* **490,** 192–200 (2012).
33. Li, B., Rooney, D. W., Zhang, N. & Sun, K. An *In Situ* Ionic-Liquid-Assisted Synthetic Approach to Iron Fluoride/Graphene Hybrid Nanostructures as Superior Cathode Materials for Lithium Ion Batteries. *Acs Appl Mater Inter* **5,** 5057–5063 (2013).
34. Buqa, H., Goers, D., Holzapfel, M., Spahr, M. E. & Novák, P. High Rate Capability of Graphite Negative Electrodes for Lithium-Ion Batteries. *J Electrochem Soc* **152,** A474–A481 (2005).
35. Hameed, A. S. *et al.* Room temperature large-scale synthesis of layered frameworks as low-cost 4V cathode materials for lithium ion batteries. *Sci Rep-Uk* **5,** 16270 (2015).
36. Shen, Y. *et al.* Sheet-like structure FeF3/graphene composite as novel cathode material for Na ion batteries. *Rsc Adv* **5,** 38277–38282 (2015).
37. Reddy, M. V. *et al.* Studies on the lithium ion diffusion coefficients of electrospun Nb2O5 nanostructures using galvanostatic intermittent titration and electrochemical impedance spectroscopy. *Electrochim Acta* **128,** 198–202 (2014).
38. Wu, Y., Reddy, M. V., Chowdari, B. V. R. & Ramakrishna, S. Electrochemical studies on electrospun Li(Li1/3Ti5/3)O4 grains as an anode for Li-ion batteries. *Electrochim Acta* **67,** 33–40 (2012).
39. Ravel, B. & Newville, M. Athena, Artemis, HephaestuS: data analysis for X-ray absorption spectroscopy using IFEFFIT. *J Synchrotron Radiat* **12,** 537–541 (2005).

Acknowledgements

Author Contributions

G.A. conceived the experiments, fabricated the devices, carried out X-ray absorption spectroscopy measurements and analyzed the results. J.-H.L., W.C., B.-W.C., H.-G.J. and K.-W.N. helped to write and arrange the manuscript. K.Y.C. supervised this work throughout the experiments, discussions and writing the manuscript.

Additional Information

Competing financial interests: The authors declare no competing financial interests.

How to cite this article: Ali, G. *et al.* Lithium intercalation mechanism into FeF$_3$·0.5H$_2$O as a highly stable composite cathode material. *Sci. Rep.* **7**, 42237; doi: 10.1038/srep42237 (2017).

Publisher's note: Springer Nature remains neutral with regard to jurisdictional claims in published maps and institutional affiliations.